Available online at www.sciencedirect.com
ScienceDirect
Journal of Sound and Vibration 323 (2009) 232–256
JOURNAL OF SOUND AND VIBRATION
www.elsevier.com/locate/jsvi

Flexural self-damping in overhead electrical transmission conductors

Charles B. Rawlins*

16 Riverside Parkway, Massena, NY 13662, USA

Received 16 April 2008; received in revised form 17 December 2008; accepted 18 December 2008
Handling Editor: S. Bolton
Available online 31 January 2009

Abstract

Internal damping of tensioned cables during flexure by transverse vibration is analyzed. The flexure causes relative movements between the wires or strands of the cable, movements which are constrained by friction between them. Under conditions common to vibration of overhead transmission line conductors the friction is great enough to prevent gross sliding. However, there is microslip at the edges of the interstrand contacts, so there is frictional dissipation. In addition, the frictional forces cause shear strains at the contacts with resulting material damping. An analysis is presented that connects the bodily flexure of the conductor with the internal interstrand movements and forces, and with the amounts of dissipation that occur—self-damping. Comparison of estimates based on the analysis with measured data on self-damping reveals reasonable agreement, for a limited range. Cases lying outside that range appear to be associated with treatments applied to cable samples involved in the measurements prior to testing. Possible mechanisms activated by these treatments are discussed.

1. Introduction

The cables of overhead electric power lines are subject under wind action to vortex-induced vibration, known in the electrical industry as "aeolian vibration." The motion takes the form of vibration waves. Fatigue of cable elements can occur at locations such as at supporting towers, where reflection of these waves causes concentrated localized flexure of the conductor.

Severity of the vibration is determined by the balance among the vortex-driven power supplied by the wind, the power dissipated within the conductor, and that dissipated by external sources such as attached dampers and losses in supporting structures [1]. There is extensive information on the power imparted by the wind to vibrating cables, or to cylinders that model them [2]. There is also well-developed technology for measuring dissipation by attached external dampers [3]. Dissipation in supporting structures is usually small, and very difficult to predict when it is not, so it is generally ignored in power balance calculations.

*Tel.: +1 315 764 0817; fax: +1 315 769 6740.
E-mail address: rawlins@ieee.org

0022-460X/$ - see front matter © 2008 Elsevier Ltd. All rights reserved.
doi:10.1016/j.jsv.2008.12.022

Nomenclature

a	major axis of contact ellipse
A	cross sectional area of strand
b	minor axis of contact ellipse; width of line contact
B_0, B_1	specific damping coefficients; see Eqs. (94) and (95).
c	transverse wave velocity
C	contact compliance
C_E	see Eq. (14)
d	strand diameter
D	conductor diameter
e	eccentricity of contact ellipse
E	Young's modulus
EI	cable flexural rigidity
f	vibration frequency
F	traction force on contact, referred to strand axis; see Fig. 9
$\mathscr{F}$	traction force referred to principle axes of contact; see Fig. 9
g	dimensionless relative normal approach of contacting strands
G	shear modulus
h	relative normal approach of contacting strands
H	cable tension
i	index to strands in a layer
j	index to helical layers; for innermost, $j=1$
J	hysteritic dissipation per cycle
k	eccentricity of contact ellipse
K_D	see Eq. (14)
$\mathscr{K}$	dimensionless curvature of conductor
m	cable mass per unit length
M	bending moment due to interstrand tractions
n_i	number of strands in layer i
N	number of helical layers in cable
$\tilde{N}_{i,j}$	number of contacts per unit length of a strand of layer i with strands of layer j
$N_{j,j+1}$	number of interlayer contacts between j and $j+1$ per unit length of conductor
N_S	Strouhal number
p	dimensionless major axis of contact ellipse
P	normal load on contact
q	dimensionless minor axis of contact ellipse
Q	see Eq. (72)
r	radius of helix defining strand axis
RS	rated conductor strength
s	coordinate embedded in strand axis
S_j	total inward force per unit length on layer j
t	time
T	strand tension
u	tangential relative displacement at elliptical contact
U	stored elastic energy
V	wind velocity
w	amplitude of cable in y direction
$w_{\max}$	mid-loop single amplitude
W	frictional dissipation per cycle
x	coordinate embedded in the cable axis
y	coordinate normal to cable axis in plane of bending (see Fig. 7)
z	coordinate normal to cable axis transverse to plane of bending (see Fig. 7)
Z	see Eq. (70)
α	lay angle of strand axis
β	angle between strand axis and principle axis of contact
γ	see Eq. (18)
Γ	function defined in Eq. (20)
δ	displacement of strand parallel to its axis
ε	strain
η	displacement of strand normal to its axis
θ	angular position of strand in conductor cross section
κ	curvature of cable axis at mid-loop
λ	lay length of helical strand
μ	coefficient of friction
ν	Poisson's ratio
ξ	see Eq. (16)
ρ	angular position of intralayer interstrand contact
σ	frictional loss tangent for parallel strands
τ	curvature of strand due to helicity
ϕ	difference in lay angles of adjacent layers, $\lvert\alpha_j\rvert + \lvert\alpha_{j+1}\rvert$
ψ	specific damping capacity of material
Ψ	specific damping capacity of conductor stiffness
ω	circular frequency
$\hat{\square}$	indicates maximum value within a layer
$\bar{\square}$	indicates mean value
$\tilde{\square}$	indicates distributed form of discrete function

Dissipation within the conductor, "self damping," is determined through measurements in the laboratory, where relatively short spans, generally in the range 50–100 m, are vibrated at various frequencies and amplitudes that may occur in the field, and dissipation within the conductor is measured. The measurements are difficult and time consuming and, although procedures for making them are described in certain standards [4,5], there is wide scatter among test results from different laboratories and, indeed, from within the same laboratory, even for identical conductors. Some of this dispersion is certainly due to the difficulty of measurement. The levels of vibration power involved are small. Some dispersion may result from departures from procedures recommended in standards. However, some of it may well be associated with variations in characteristics of the conductor samples, characteristics whose importance has not been recognized, or which have not been considered feasible to determine. This latter possibility points to the need for a suitable analytical model of conductor self damping mechanics. The purpose of this paper is to propose such a model for use as a tool for exploring and better understanding those characteristics. It will be applied for that purpose in Section 5 where its predictions will be compared with several sets of laboratory measurements of self damping.

As noted above, overhead conductor vibration takes the form of waves. Motions are in the crosswind direction, thus generally vertical. If the stiffness of the span supports is high, the waves traveling in opposite directions along the span combine to form its eigenmodes. These may be complex when there are localized sources of dissipation such as attached dampers or loses at supports. However it is sufficient for the present discussion to focus on the case where such external damping is absent. Then the eigenmodes are real and are formed from sine-shaped loops. Thus, the lateral displacement of the cable is $w = w(x)\cos\omega t$, where

$$w(x) = w_{\max}\sin\frac{\omega x}{c}, \tag{1}$$

$w_{\max}$ is mid-loop single amplitude, ω is circular frequency of vibration, x is the coordinate embedded in the cable axis, t is time and c is transverse wave velocity. Frequencies are determined approximately by the Strouhal relation

$$f = N_S\frac{V}{D}, \tag{2}$$

where V is the component of wind velocity normal to the cable, D is cable diameter, and the Strouhal number N_S is a function of Reynolds number and the roughness of the conductor surface. For the range of interest for overhead conductors it has a value of approximately 0.185. Vibration of field spans usually shows the simultaneous presence of several eigenmodes with frequencies clustered around that expected on the basis of Eq. (2), leading to complexities that are beyond the scope of the paper. Thus the analysis that follows considers the case where only one mode is present, represented by Eq. (1).

2. Background

Overhead conductors are manufactured as multi-strand concentric-lay cables to make them flexible so that they can be wound onto reels for shipment. Flexibility is afforded by the freedom of individual strands to slide longitudinally. Fig. 1 illustrates the direction of this sliding when a cable is given curvature κ. The sliding relieves the difference in stress—compression on the top and tension on the bottom—that would occur in a similarly bent solid bar. Conductors are stranded with the direction of lay reversed, layer-by-layer to

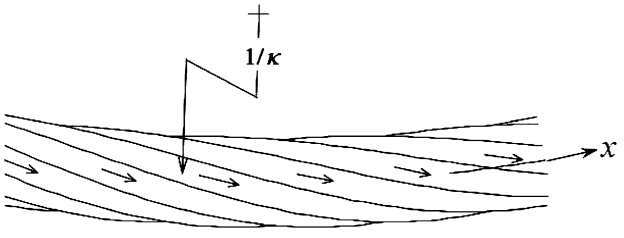

Fig. 1. Longitudinal displacement of strands during flexure.

improve their structural integrity by defining the space for each layer through a dense matrix of interlayer contacts.

When the conductor is installed in an overhead span, it is placed under significant tension which is distributed among the strands. The tensions in the helically shaped strands bind them against the layers below. Strand sliding then is confronted by friction, resulting in a large increase in conductor stiffness. It was suggested as early as 1930 that the curvature imposed on conductors by vibration could lead to frictional damping through the sliding of the strands. Ryle [6] provided the first analytical estimates of the critical curvature at which sliding would take place. When curvature exceeded this value frictional dissipation would occur and there would be hysteretic damping. Ryle did not consider effects of the longitudinal elasticity of the strands nor the tangential compliance of interstrand contacts. In fact, workable analyses of that compliance did not become available until some years later in the work of Mindlin [7], Johnson [8], Goodman [9] and others. The significance of this work to self damping technology has been described by Hardy et al. [10,11]. Briefly, the conductor strands do displace, as illustrated in Fig. 1, but the displacement relative to the layer below is accommodated in large part by elastic shear strain at the interstrand contacts. However, the normal pressure on the contact is not uniform; it tapers to zero at the edge. As a result, static friction there is overcome by the tangential stress on the contact, and sliding occurs in an annular region along the contact periphery. This region expands inward as the tangential load on the contact increases, and contracts outward as the load is reduced. During vibration, the region expands and contracts for each half cycle, and the micro-slipping that takes place results in frictional dissipation and thus conductor self damping. The analysis of Section 4 makes generous use of the work of Hardy et al. [10,11], who have already dealt with the single-layer problem.

The magnitude of that frictional dissipation per cycle for possibly different contacting materials 1 and 2 is given by Johnson as [8]

$$W = \frac{1}{36\mu P\sqrt{ab}}\left(\frac{2-\nu_1}{G_1}+\frac{2-\nu_2}{G_2}\right)F^3, \tag{3}$$

assuming that the maximum thickness of the micro-slip annulus is much smaller than a. P is the normal load on the contact, μ is friction coefficient, ν is Poisson's ratio, G is shear modulus, a and b are the major and minor semi-axes of the contact ellipse, and F is the applied traction force. Johnson [12] tested this expression against measurements of contact damping of a steel sphere against a steel plate. He found satisfactory agreement except at very low force amplitudes. There, W appeared to vary as the square, rather than the cube of force amplitude. It was suggested that internal material damping was a major cause. This damping would be associated with alternating shear stresses at the contact interface, within the no-slip region. Thus, it appears likely that there are two mechanisms at work in conductor self damping. One is microslip at the edges of the contact areas, with dissipation proportional to the cube of the traction force amplitude. The other is material damping proportional to the maximum elastic energy stored in the tangential compliance of the contact by the traction force.

Conductors are characterized by the materials of the strands, their diameters, the number of layers and the number of strands in each, and the lay lengths of the individual layers. Lay length and lay angle are defined in Fig. 2. A typical conductor is the aluminum conductor steel reinforced (ACSR) "Cardinal" with the construction listed in Table 1. It has an overall diameter of 30.38 mm, mass of 1.829 kg/m and strength of 150.35 kN. Industry standards permit some variation in lengths of lay. The values in Table 1 are based on the "preferred" lay ratios of Ref. [13]. The full ranges of permitted lay lengths are defined such that the space

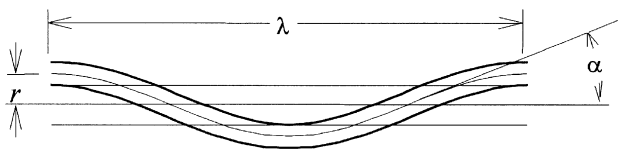

Fig. 2. Helix dimensions.

Table 1
Construction of ACSR (Cardinal).

Layer	Material	No. of strands	Strand dia. (mm)	Lay length λ (m)
4	Aluminum	24	3.376	0.334
3	Aluminum	18	3.376	0.307
2	Aluminum	12	3.376	0.236
1	Steel	6	3.376	0.243
0	Steel	1	3.376	–

allowed for the strands of a layer is never quite filled [14]. Exceptions occur for layers of seven strands, where fill ratios can exceed unity for some lay lengths, and for 6-strand layers where that is always the case.

3. Approximations

(a) The analysis assumes that the areas of the annuli of microslip are small enough compared to the areas of contact that the elastic compliance of the contacts is not affected. Then the conductor behaves linearly. Stresses are proportional to strains, and the interstrand tractions at contacts are proportional to the distortion of the conductor, i.e. its curvature.

(b) Conductor curvature is assumed to remain constant over the length of lay in any layer. From (1), curvature is,

$$\frac{d^2w}{dx^2} = -w_{max}\frac{\omega^2}{c^2}\sin\frac{\omega x}{c}, \tag{4}$$

where wave velocity is given by [15],

$$c = \sqrt{\frac{H}{m}}\sqrt{\frac{1}{2}+\sqrt{\frac{1}{4}+4\pi^2 f^2\frac{m\cdot EI}{H^2}}}, \tag{5}$$

where H is the tension in the cable, m is its unit mass, and EI is its flexural rigidity. The value of the second radical remains close to unity for conditions encountered in aeolian vibration. The deviations from unity are useful for determining the actual flexural rigidity EI from laboratory measurements of wave length as a function of frequency. For "Cardinal" ACSR at a tension of 25 percent of its rated strength, $c \approx 236$ m/s. Now, as a matter of observation, aeolian vibration is almost never observed in winds greater than 10 m/s. At that wind speed for "Cardinal", Eq. (2) indicates a frequency of 61 Hz. The wave length would be $c/f = 3.86$ m. At lower wind speeds the wave length would be greater. Thus, referring to Table 1, the lay lengths of the strands would be one-tenth or less of the wave length. Focusing on the middle of the sine-shaped loop of Eq. (4), one tenth of the wave length would encompass $\pm 18^\circ$ about the 90° point. The sine function would then remain between 0.95 and 1.00.

(c) Interstrand tractions between layers are applied to a strand at discrete points along its length, where it crosses the strands of the layer above or below. At a certain point it is helpful to represent this array of discrete tractions with a continuous traction function. The density of contacts within a lay length affects the soundness of that substitution. The number of contacts in a lay length of Layer a with strands of Layer b is,

$$m_{ab} = n_b\left(1+\frac{\lambda_a}{\lambda_b}\right), \tag{6}$$

in which n_b is the number of strands in Layer b and λ is the lay length. Referring to Table 1, the lowest density, about 12, occurs in the contacts of the 12-strand layer with the 6-strand layer. The angular increment between contacts is about 30°. The impact of this large increment is reduced by the fact that there are 12 strands in Layer a in this example, so there are about 144 contacts between the 6- and 12-strand layers within a lay length of the 12-strand layer.

4. Analysis

4.1. Normal loads at contacts between layers

The dimensions of the contact area and the elastic properties of the contacting materials determine tangential compliance at contacts. The normal loads at the contact determine the contact dimensions. These normal loads are created by inward pressure by strands due to their combination of static tension and curvature. This curvature for a helical strand is

$$\tau = \frac{\sin^2 \alpha}{r}, \tag{7}$$

where α is the lay angle of the strand axis and r is the helix radius to that axis. The inward pressure per unit length of strand is $Y = T\tau$, where T is the tension in the strand. Then the total inward force originating in a layer per unit length of *conductor* is

$$nT\frac{\sin^2 \alpha}{r \cos \alpha}. \tag{8}$$

Each layer except the outer layer transmits the pressure from layers above it through to layers below. Thus, in a conductor of N helical layers, the force on layer $j<N$ is

$$S_j = \sum_{j}^{N} \frac{n_i T_i \sin^2 \alpha_i}{r_i \cos \alpha_i}. \tag{9}$$

The total number of contacts between layer j and the layer above it is

$$N_{j,j+1} = n_j n_{j+1}\left(\frac{1}{\lambda_j} + \frac{1}{\lambda_{j+1}}\right). \tag{10}$$

Thus, the normal load per contact between layers j and $j+1$ is

$$P_{j,j+1} = \frac{1}{n_j n_{j+1}}\left(\frac{1}{\lambda_j} + \frac{1}{\lambda_{j+1}}\right)^{-1} \sum_{i=j}^{N} \frac{n_i T_i \sin^2 \alpha_i}{r_i \cos \alpha_i}. \tag{11}$$

Note that the layers are not self-supporting through *intralayer* interstrand pressures since layer fill ratios are less than unity. The 6-strand layer is an exception. Since the space within that layer is always larger than the center strand, the force from all helical layers is borne by pressure *between* the strands of the 6-strand layer. It can be shown that this pressure, per unit length of contact is

$$P_{1,1} = \frac{S_1}{6}\frac{1}{\sqrt{1 + \frac{3}{16\pi^2}\tan^2 \alpha_1}}. \tag{12}$$

4.2. Contact characteristics

Hertzian contact between non-parallel cylindrical bodies results in an elliptical contact area. Its dimensions are determined by the diameters of the cylinders, the angle between their axes, their elastic properties and the normal load on the contact. The major and minor semi-axes are given by, respectively [16],

$$a = p(PK_D C_E)^{1/3}, \quad b = q(PK_D C_E)^{1/3}, \tag{13}$$

where, P is the normal force on the contact:

$$K_D = \frac{0.75}{\frac{1}{d_1} + \frac{1}{d_2}}, \quad C_E = \frac{1 - v_1^2}{E_1} + \frac{1 - v_2^2}{E_2}, \tag{14}$$

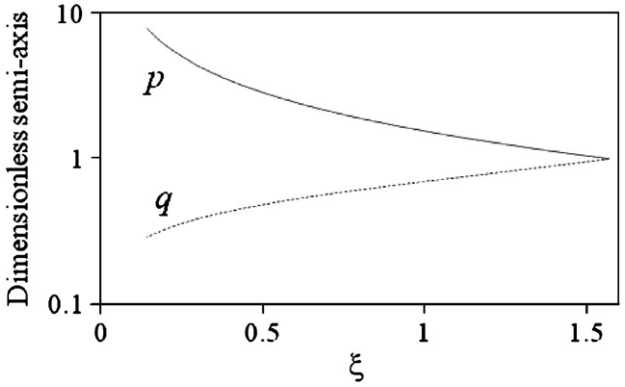

Fig. 3. Dimensionless ellipse semi-axes. Solid—major axis p; dashed—minor axis q.

where d is strand diameter and E is Young's modulus. The relative approach of contacting strands is given by

$$h = g(P^2 C_E^2 / K_D)^{1/3} \tag{15}$$

p, q and g are functions of an angle ξ. p and q are illustrated in Fig. 3. ξ is found from

$$\cos\,\xi = \frac{K_D}{1.5}\sqrt{\frac{4}{d_1^2}+\frac{4}{d_2^2}+\frac{8}{d_1 d_2}\cos\,2\phi}, \tag{16}$$

where ϕ is the angle between the cylinder axes. If $d_1 = d_2$, $\xi = \phi$. Although curvature τ of the cylinders can also influence the contact dimensions, it is small enough that conductor strands may be considered locally straight. Eqs. (14) and (16) reflect that simplification. ξ is related to the eccentricity e of the contact ellipse through the relation

$$\cos\,\xi = \frac{e^2}{2-e^2}. \tag{17}$$

The functions p and q are given in tabular form in Ref. [16], but are made available as polynomials in ϕ in Appendix A, applicable to the range of ξ found in conductors. When the contacting strands are of equal diameter, the major principal axis of the contact ellipse bisects the angle between the axes of the two strands. When the strand diameters are different, the major principle axis of the ellipse is rotated toward the axis of the smaller strand. It can be shown from Ref. [17] that this rotation is

$$\gamma_{12} = \frac{1}{2}\arctan\left(\frac{\sin\,2\phi_{12}}{\frac{d_2}{d_1}+\cos\,2\phi_{12}}\right) - \frac{\phi_{12}}{2} \tag{18}$$

where $d_2 > d_1$.

The average stress on the contact interface is simply $\sigma_n = P/\pi ab$. It is found that in practice this stress is substantially greater than the bearing yield stress for the aluminum alloy used in most overhead conductors, 1350-H19. Elastic–plastic modeling of contact indentation [8] suggests that this yield stress should be about $3Y$, where Y is the yield stress in tension or compression. For 1350-H19, $Y \approx 100$ MPa. Thus the average contact stress is expected to be about 300 MPa. Indeed, measurements by the author of contact dimensions under different loads correlate well with this value when the crossing angle is 90°, as shown in Fig. 4. For the crossing angles that occur in overhead conductors, 10°–30° however, the average stress is more nearly 240 MPa.

Yielding of the contact expands the contact area. For purposes of this study, the shape of the contact ellipse is assumed to remain that found for the Hertz contact. In addition, it is assumed that once yielding occurs the average stress over the contact area is equal to the bearing yield stress, thus determining the area of the yielded contact. Yielding of the contact also increases the relative approach of the contacting strands. Again for

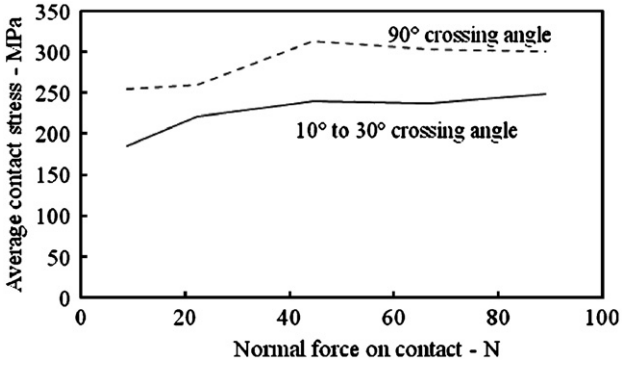

Fig. 4. Average contact stress under yield for 3.68 mm strands of 1350-H19 aluminum. Dashed—90° crossing angle; solid—10° to 30° crossing angles.

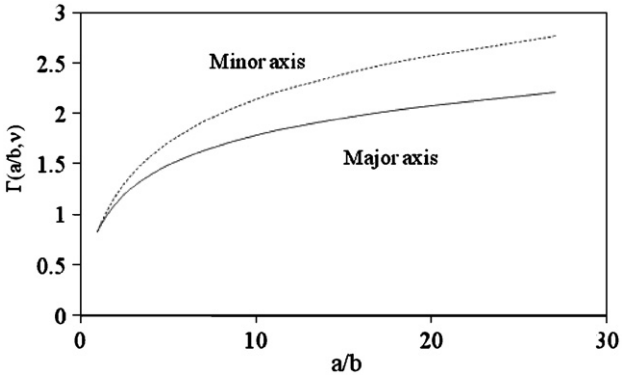

Fig. 5. Tangential compliance functions. Solid—parallel to ellipse major axis; dashed—parallel to ellipse minor axis. $v = 0.33$.

purposes of this study, that approach is estimated using the plausible but unproven model that h varies in proportion to contact area during yielding.

As noted earlier, most of the relative tangential displacement of contacting strands is absorbed in elastic shear strain at the interfaces. This elastic behavior is characterized by tangential compliance, the ratio of the relative displacement to the tangential shear force causing it, $C = u/F$. When the contact is elliptical the compliances in the directions of the two principal axes are different. If both strands are of the same material, they are given by Ref. [18]

$$\frac{u}{F} = \frac{1}{2Ga}\Gamma\left(\frac{a}{b}, v\right), \tag{19}$$

where,

$$\Gamma\left(\frac{a}{b}, v\right) = \frac{2-v}{2}\left[\frac{2K(k)}{\pi} \pm \frac{v}{2\pi^2(2-v)}\frac{N(k)}{k}\right] \tag{20}$$

and

$$N(k) = 4\pi\left[\left(\frac{2}{k} - k\right)K(k) - \frac{2}{k}E(k)\right]. \tag{21}$$

K and E are the complete elliptic integrals of the first and second kind of argument $(\pi/2, k)$ where $k^2 = 1 - b^2/a^2$. In Eq. (20), the $(+)$ option applies to u and F in the b direction and $(-)$ to u and F in the a direction. The Γ functions are shown in Fig. 5 and are presented as polynomials in a/b in Appendix A for the case where $v = 0.33$.

When the contacting strands are of different materials,

$$C_{j,j+1} = \frac{1}{4G_j a}\Gamma\left(\frac{a}{b}, \nu_j\right) + \frac{1}{4G_{j+1}a}\Gamma\left(\frac{a}{b}, \nu_{j+1}\right). \tag{22}$$

As noted in Section 4.1, the innermost helical layer is self-supporting through pressure between its strands. The interstrand contacts take the form of narrow strips of width b. For Hertzian contact [8],

$$b^2 = \frac{2dP_{1,1}(1-\nu^2)}{\pi E}. \tag{23}$$

It has been shown [19] that the longitudinal compliance at such contacts is

$$C_x = \frac{b^2}{dP_{1,1}(1-\nu)}\left(\ln\frac{2d}{b} - \frac{1}{2}\right) - \frac{1}{2\pi G}. \tag{24}$$

However, measured values of C_x for aluminum strands were found to be roughly twice theoretical values. It was suggested that roughness of mill quality strands may have been responsible.

4.3. Strand displacements

When the conductor is flexed to curvature κ, the strands tend to displace longitudinally, as illustrated in Fig. 6. At the point of maximum displacement, curvature at mid-loop is

$$\kappa = \frac{4\pi^2 f^2 w_{\max}}{c^2}. \tag{25}$$

These displacements are functions of position along the strand. Let the strands in a layer be numbered as in Fig. 7. When the curvature is constant along the conductor, the displacements will be greatest where $\theta = 0$ or

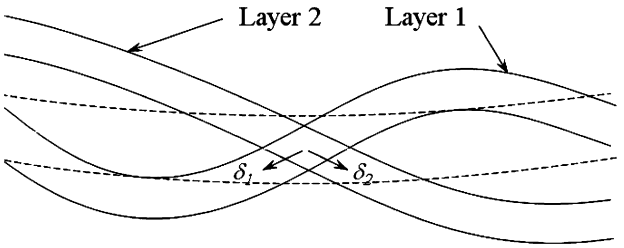

Fig. 6. Positive longitudinal displacements of strands during positive flexure.

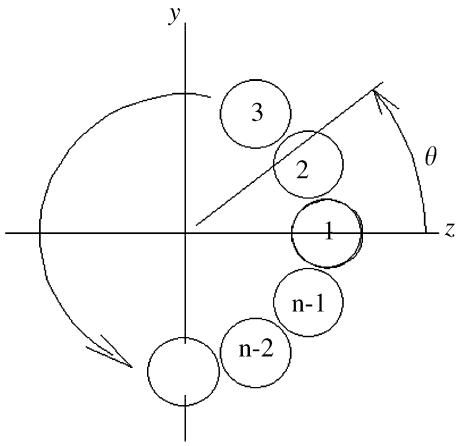

Fig. 7. Strand numbering (at $x = 0$).

π, and will be zero where $\theta = \pm\pi/2$. Thus the displacements may reasonably be assumed to take the form

$$\delta = \hat{\delta} \cos \theta. \tag{26}$$

Displacement δ of a point along a strand is measured with respect to the position it would occupy if the conductor flexed as a solid bar. Thus, when all interstrand contact compliances are taken to be zero, $\delta = 0$ everywhere.

Now the helical axis of the ith strand takes the form

$$y_i = r \sin \theta_i, \quad z_i = r \cos \theta_i, \tag{27}$$

where

$$\theta_i = 2\pi\left(\frac{i-1}{n} \pm \frac{x}{\lambda}\right). \tag{28}$$

The $(-)$ option pertains to right-hand pitch and $(+)$ to left-hand pitch. For the case where the conductor is flexed in the y direction to a curvature κ, and where $\delta = 0$, the strand experiences a strain $-\kappa y$ in the direction normal to the conductor cross section. The strain of the strand along its axis is then $-\kappa y \cos^2 \alpha$. If this strain is released by allowing the strands to slide freely, displacements δ_f occur such that

$$\delta_{fi} = \kappa \cos^2 \alpha \int y_i \, \mathrm{d}s = \frac{\kappa r \lambda}{2\pi} \cos \alpha \cos \theta_i, \tag{29}$$

where s is the coordinate embedded in the strand axis. Note that $\mathrm{d}s = \mathrm{d}x/\cos\alpha$ and $\mathrm{d}x = (\lambda/2\pi)\,\mathrm{d}\theta$. The integration in Eq. (29) is carried from the top of the helix where $\theta = \pi/2$ to θ_i.

It is important to note that strands may experience lateral displacements η as well as longitudinal displacements δ. The layers of strands in overhead conductors are not tightly packed, i.e. they do not completely fill the circumferential space provided for them when the conductor is manufactured in compliance with industry standards [13,20], except for the first layer above the core strand. Thus, the total displacement has two components as illustrated in Fig. 8 for each of the two strands engaged in contact. The strands of the innermost helical layer are well-packed so $\eta = 0$ throughout that layer.

4.4. Tractions at interlayer contacts

The relative displacements across interlayer contacts determine the traction force $\mathscr{F}$ that is transmitted. This force is conveniently resolved into components $\mathscr{F}_a$ and $\mathscr{F}_b$ along the major and minor axes of the contact ellipse. The contact compliances in those two directions are given by Eq. (19) and are denoted

$$C_a = \delta/\mathscr{F}_a, \quad C_b = \eta/\mathscr{F}_b. \tag{30}$$

The total traction $\mathscr{F}$ is the vector sum of $\mathscr{F}_a$ and $\mathscr{F}_b$. Denote the force by strand 1 upon the contact as $\mathscr{F}_{12}$, and that by strand 2 on the contact as $\mathscr{F}_{21}$. These can be resolved into components longitudinal and lateral to strands 1 and 2 as illustrated in Fig. 9.

Fig. 9 was constructed with the major principle axis of the contact ellipse parallel to the conductor axis. Actually, if $\alpha_1 \neq \alpha_2$, the ellipse is tilted by $|\alpha_1| - |\alpha_2|$, and if the diameters of the contacting strands are not

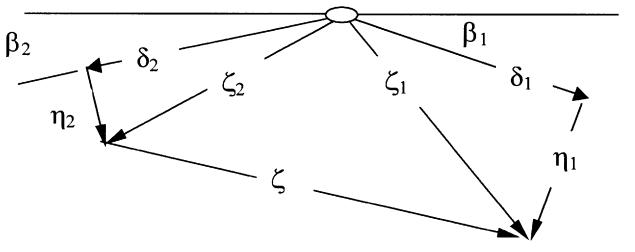

Fig. 8. Displacements of two strands in contact.

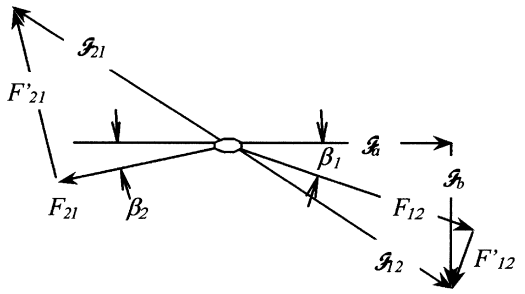

Fig. 9. Forces on interstrand contact.

equal it will be tilted further by γ_{12}. For the lay angle and strand diameters found in overhead conductors, however, these deviations are small enough to neglect.

Referring to Figs. 8 and 9, we find

$$\mathscr{F}_{a12} = \frac{1}{C_{a12}}(\delta_1 \cos\alpha_1 - \eta_1 \sin\alpha_1 + \delta_2 \cos\alpha_2 - \eta_2 \sin\alpha_2), \tag{31}$$

$$\mathscr{F}_{b12} = \frac{1}{C_{b12}}(\eta_1 \cos\alpha_1 + \delta_1 \sin\alpha_1 - \eta_2 \cos\alpha_2 - \delta_2 \sin\alpha_2), \tag{32}$$

$$F_{12} = \mathscr{F}_{a12}\cos\alpha_1 + \mathscr{F}_{b12}\sin\alpha_1, \quad F_{21} = \mathscr{F}_{a12}\cos\alpha_2 + \mathscr{F}_{b12}\sin\alpha_2, \tag{33}$$

$$F'_{12} = \mathscr{F}_{b12}\cos\alpha_1 - \mathscr{F}_{a12}\sin\alpha_1, \quad F'_{21} = \mathscr{F}_{b12}\cos\alpha_2 + \mathscr{F}_{a12}\sin\alpha_2. \tag{34}$$

The subscripts for $\mathscr{F}$, C_a and C_b have been extended to indicate that they pertain to contacts between layers 1 and 2. Correspondingly, the forces between layers 2 and 3 may be written

$$\mathscr{F}_{a23} = \frac{1}{C_{a23}}(\delta_2 \cos\alpha_2 - \eta_2 \sin\alpha_2 + \delta_3 \cos\alpha_3 - \eta_3 \sin\alpha_3), \tag{35}$$

$$\mathscr{F}_{b23} = \frac{1}{C_{b23}}(\eta_2 \cos\alpha_2 + \delta_2 \sin\alpha_2 - \eta_3 \cos\alpha_3 - \delta_3 \sin\alpha_3), \tag{36}$$

$$F_{23} = \mathscr{F}_{a23}\cos\alpha_2 + \mathscr{F}_{b23}\sin\alpha_2, \quad F_{32} = \mathscr{F}_{a23}\cos\alpha_3 + \mathscr{F}_{b23}\sin\alpha_3, \tag{37}$$

$$F'_{23} = \mathscr{F}_{b23}\cos\alpha_2 - \mathscr{F}_{a23}\sin\alpha_2, \quad F'_{32} = \mathscr{F}_{b23}\cos\alpha_3 + \mathscr{F}_{a23}\sin\alpha_3. \tag{38}$$

Note that δ_1, δ_2, η_1, η_2 are all assumed to share the same angular position θ in Eqs. (31) and (32), and δ_2, δ_3, η_2, η_3 to do so in Eqs. (35) and (36).

It is convenient to put these forces in distributed form, i.e. as force per unit length of strand. That can be done by multiplying them by the number of contacts per unit length. The number of contacts of a strand of layer 2 with layer 1 and with layer 3 are, respectively,

$$\tilde{N}_{21} = n_1\left(\frac{1}{\lambda_1}+\frac{1}{\lambda_2}\right)\cos\beta_2, \quad \tilde{N}_{23} = n_3\left(\frac{1}{\lambda_2}+\frac{1}{\lambda_3}\right)\cos\beta_2. \tag{39}$$

Then the total traction per unit length upon a strand in layer 2 from layers 1 and 3, parallel and transverse to that strand, amount to, respectively,

$$\tilde{F}_2 = \tilde{N}_{21}F_{12} + \tilde{N}_{23}F_{23}, \quad \tilde{F}'_2 = \tilde{N}_{21}F'_{12} + \tilde{N}_{23}F'_{23}, \tag{40}$$

where it is now assumed that all of δ_1, δ_2, δ_3, η_1, η_2 and η_3 share the same θ and $\tilde{F}_2$ and $\tilde{F}'_2$ are functions of that value. $\tilde{F}_2$ induces a gradient in strand tension that will be addressed below. Since there is no pressure between the strands of layer 2, $\tilde{F}'_2 = 0$.

Substitution of Eqs. (31)–(39) into Eq. (40) yields polynomials in δ_1, δ_2, δ_3, η_1, η_2 and η_3. These may be expressed as

$$\tilde{F}_2 = X_1\delta_1 + X_2\delta_2 + X_3\delta_3 + X_4\eta_1 + X_5\eta_2 + X_6\eta_3, \tag{41}$$

$$\tilde{F}'_2 = Y_1\delta_1 + Y_2\delta_2 + Y_3\delta_3 + Y_4\eta_1 + Y_5\eta_2 + Y_6\eta_3, \tag{42}$$

where

$$X_1 = \tilde{N}_{21}\left(\frac{\cos\alpha_1\cos\alpha_2}{C_{a12}} - \frac{\sin\alpha_1\sin\alpha_2}{C_{b12}}\right), \tag{43}$$

$$X_2 = \left(\frac{\tilde{N}_{21}}{C_{a12}} + \frac{\tilde{N}_{23}}{C_{a23}}\right)\cos^2\alpha_2 + \left(\frac{\tilde{N}_{21}}{C_{b12}} - \frac{\tilde{N}_{23}}{C_{b23}}\right)\sin^2\alpha_2, \tag{44}$$

$$X_3 = \tilde{N}_{23}\left(\frac{\cos\alpha_2\cos\alpha_3}{C_{a23}} - \frac{\sin\alpha_2\sin\alpha_3}{C_{b23}}\right), \tag{45}$$

$$X_4 = -\tilde{N}_{21}\left(\frac{\sin\alpha_1\cos\alpha_2}{C_{a12}} + \frac{\cos\alpha_1\sin\alpha_2}{C_{b12}}\right), \tag{46}$$

$$X_5 = -\left[\tilde{N}_{21}\left(\frac{1}{C_{a12}} - \frac{1}{C_{b12}}\right) + \tilde{N}_{23}\left(\frac{1}{C_{a23}} - \frac{1}{C_{b23}}\right)\right]\sin\alpha_2\cos\alpha_2, \tag{47}$$

$$X_6 = -\tilde{N}_{23}\left(\frac{\sin\alpha_3\cos\alpha_2}{C_{a23}} + \frac{\cos\alpha_3\sin\alpha_2}{C_{b23}}\right), \tag{48}$$

$$Y_1 = \tilde{N}_{21}\left(\frac{\sin\alpha_1\cos\alpha_2}{C_{b12}} + \frac{\cos\alpha_1\sin\alpha_2}{C_{a12}}\right), \tag{49}$$

$$Y_2 = -X_5, \tag{50}$$

$$Y_3 = \tilde{N}_{23}\left(\frac{\sin\alpha_3\cos\alpha_2}{C_{b23}} + \frac{\cos\alpha_3\sin\alpha_2}{C_{a23}}\right), \tag{51}$$

$$Y_4 = \tilde{N}_{21}\left(\frac{\cos\alpha_1\cos\alpha_2}{C_{b12}} - \frac{\sin\alpha_1\sin\alpha_2}{C_{a12}}\right), \tag{52}$$

$$Y_5 = -\left(\frac{\tilde{N}_{21}}{C_{a12}} + \frac{\tilde{N}_{23}}{C_{a23}}\right)\sin^2\alpha_2 - \left(\frac{\tilde{N}_{21}}{C_{b12}} + \frac{\tilde{N}_{23}}{C_{b23}}\right)\cos^2\alpha_2, \tag{53}$$

$$Y_6 = \tilde{N}_{23}\left(\frac{\cos\alpha_2\cos\alpha_3}{C_{b23}} - \frac{\sin\alpha_2\sin\alpha_3}{C_{a23}}\right). \tag{54}$$

The analysis above focused on layers 1, 2 and 3, but it can be generalized by substituting $j-1$, j and $j+1$ for those values. The coefficients X and Y above may then be applied to a generic layer j by incorporating those substitutions. The tractions within the innermost layer arise from the relative displacements of adjacent strands of the layer. For strand i of that layer, the traction from both sides is (see Fig. 10):

$$F_i = \frac{\delta_{i+1} - \delta_i}{C_x} + \frac{\delta_{i-1} - \delta_i}{C_x} = -\frac{2\delta_i - \delta_{i-1} - \delta_{i+1}}{C_x}. \tag{55}$$

From Eqs. (26) and (28),

$$\delta_i = \hat{\delta}\cos 2\pi\left(\frac{i-1}{n} \pm \frac{x}{\lambda}\right). \tag{56}$$

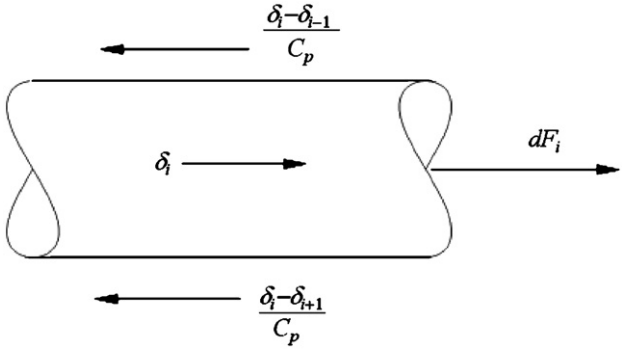

Fig. 10. Forces on innermost layer strand element.

It can be shown that

$$2\delta_i - \delta_{i-1} - \delta_{i+1} = 2\hat{\delta}\left(1 - \cos\frac{2\pi}{n}\right)\cos\,2\pi\left(\frac{i-1}{n} \pm \frac{x}{\lambda}\right). \tag{57}$$

Thus,

$$F_i = -\frac{2\hat{\delta}}{C_x}\left(1 - \cos\frac{2\pi}{n}\right)\cos\,2\pi\left(\frac{i-1}{n} \pm \frac{x}{\lambda}\right). \tag{58}$$

4.5. Determination of strand displacements

The tractions at the interstrand contacts cause increments in strand tension T. Let

$$T = \overline{T} + \Delta T. \tag{59}$$

Since the strand is longitudinally elastic, tension variation ΔT is accompanied by a longitudinal strain $\varepsilon = \Delta T/EA$ in which A is strand area. For layer 2, ΔT_2 results from the accumulation of the longitudinal tractions F_{12}, F_{32} of Eqs. (33) and (37). $\tilde{F}_2$ from Eq. (40) represents this collection of tractions as a continuous function which causes a gradient $-\mathrm{d}\Delta T_2/\mathrm{d}s_2$ in ΔT_2. Then,

$$\frac{\mathrm{d}\varepsilon_2}{\mathrm{d}s_2} = \frac{1}{EA}\frac{\mathrm{d}\,\Delta T_2}{\mathrm{d}s_2} = -\frac{1}{EA}\tilde{F}_2. \tag{60}$$

Since $\mathrm{d}x = \cos\,\alpha_2\,\mathrm{d}s_2$,

$$\frac{\mathrm{d}\varepsilon_2}{\mathrm{d}x} = -\frac{1}{EA\,\cos\,\alpha_2}\tilde{F}_2. \tag{61}$$

Denoting as $\delta_{\varepsilon 2}$ the longitudinal displacement associated with ε_2, the total longitudinal displacement is $\delta_2 = \delta_{f2} + \delta_{\varepsilon 2}$. Then,

$$\varepsilon_2 = \cos\,\alpha_2\frac{\mathrm{d}}{\mathrm{d}x}(\delta_{f2} - \delta_2). \tag{62}$$

Then, differentiating Eq. (62) and substituting from Eqs. (61) and (41),

$$\frac{\mathrm{d}^2}{\mathrm{d}x^2}(\delta_{f2} - \delta_2) = -\frac{X_1\delta_1 + X_2\delta_2 + X_3\delta_3 + X_4\eta_1 + X_5\eta_2 + X_6\eta_3}{EA\cos^2\alpha_2}. \tag{63}$$

From Eq. (29),

$$\frac{\mathrm{d}^2\delta_{f2}}{\mathrm{d}x^2} = -\frac{\kappa r_2\lambda_2}{2\pi}\cos\,\alpha_2\,\cos\,\theta_2\left(\frac{\mathrm{d}\theta_2}{\mathrm{d}x}\right)^2 = -2\pi\frac{\kappa r_2}{\lambda_2}\cos\,\theta_2. \tag{64}$$

Combining Eqs. (63) and (64),

$$\frac{d^2\delta_2}{dx^2} - \frac{X_1\delta_1 + X_2\delta_2 + X_3\delta_3 + X_4\eta_1 + X_5\eta_2 + X_6\eta_3}{EA\cos^2\alpha_2} = -2\pi\frac{\kappa r_2}{\lambda_2}\cos\alpha_2\cos\theta_2. \tag{65}$$

But, since curvature κ is constant, δ_2 must vary sinusoidally with θ_2:

$$\frac{d^2\delta_2}{dx^2} = -\frac{4\pi^2}{\lambda_2^2}\delta_2. \tag{66}$$

Thus,

$$\frac{4\pi^2}{\lambda_2^2}\delta_2 + \frac{X_1\delta_1 + X_2\delta_2 + X_3\delta_3 + X_4\eta_1 + X_5\eta_2 + X_6\eta_3}{EA\cos^2\alpha_2} = 2\pi\frac{\kappa r_2}{\lambda_2}\cos\alpha_2\cos\theta_2. \tag{67}$$

For brevity, let

$$J_l = X_l/EA\cos^2\alpha_2, \quad K_l = Y_l/EA\cos^2\alpha_2, \quad l = 1\ldots6. \tag{68}$$

Further, to generalize, let layers 1, 2 and 3 become $j-1$, j and $j+1$. Then Eq. (67) becomes

$$\frac{4\pi^2}{\lambda_j^2}\delta_j + J_1\delta_{j-1} + J_2\delta_j + J_3\delta_{j+1} + J_4\eta_{j-1} + J_5\eta_j + J_6\eta_{j+1} = Z_j, \tag{69}$$

where

$$Z_j = 2\pi\frac{\kappa r_j}{\lambda_j}\cos\alpha_j\cos\theta_j. \tag{70}$$

Recalling that there is no interstrand pressure within a layer, $\tilde{F}'_2 = 0$. Then from Eq. (42)

$$K_1\delta_{j-1} + K_2\delta_j + K_3\delta_{j+1} + K_4\eta_{j-1} + K_5\eta_j + K_6\eta_{j+1} = 0. \tag{71}$$

It is understood that the J_l and K_l are calculated for layer j.

In the case of the innermost layer, Eq. (69) must provide for the *intralayer* tractions of Eq. (58) in the form of the additional term,

$$Q = \frac{2\delta_1}{EAC_x\cos\alpha_1}\left(1 - \cos\frac{2\pi}{n_1}\right)\cos\theta_1. \tag{72}$$

Eqs. (69) and (71) can be written for each helical layer. If there are N layers, there will then be $2N$ equations. They can be made simultaneous by letting θ be the same for all layers. For convenience, let $\theta_j = 0$, for $j = 1\ldots N$. Then the set of equations can be expressed in matrix form. The result is shown in Eq. (73) for a cable with four layers.

$$\begin{bmatrix}
\frac{4\pi^2D^2}{\lambda_1^2} + J_2 + \hat{Q} & J_3 & \cdots & \cdots & J_5 & J_6 & \cdots & \cdots \\
J_1 & \frac{4\pi^2D^2}{\lambda_2^2} + J_2 & J_3 & \cdots & J_4 & J_5 & J_6 & \cdots \\
\cdots & J_1 & \frac{4\pi^2D^2}{\lambda_3^2} + J_2 & J_3 & \cdots & J_4 & J_5 & J_6 \\
\cdots & \cdots & J_1 & \frac{4\pi^2D^2}{\lambda_4^2} + J_2 & \cdots & \cdots & J_4 & J_5 \\
K_2 & K_3 & \cdots & \cdots & K_5 & K_6 & \cdots & \cdots \\
K_1 & K_2 & K_3 & \cdots & K_4 & K_5 & K_6 & \cdots \\
\cdots & K_1 & K_2 & K_3 & \cdots & K_4 & K_5 & K_6 \\
\cdots & \cdots & K_1 & K_2 & \cdots & \cdots & K_4 & K_5
\end{bmatrix}
\begin{Bmatrix}
\hat{\delta}_1 \\ \hat{\delta}_2 \\ \hat{\delta}_3 \\ \hat{\delta}_4 \\ \hat{\eta}_1 \\ \hat{\eta}_2 \\ \hat{\eta}_3 \\ \hat{\eta}_4
\end{Bmatrix} =
\begin{Bmatrix}
\hat{Z}_1 \\ \hat{Z}_2 \\ \hat{Z}_3 \\ \hat{Z}_4 \\ 0 \\ 0 \\ 0 \\ 0
\end{Bmatrix} \tag{73}$$

Table 2
Sample results, Cardinal at 25 percent RS.

Layer	j	4	3	2	1	
Contact force	P_n	18.2	60.9	238.2		N/contact
Elastic contact to layer below	a	0.205	0.355	0.653		mm
	b	0.031	0.043	0.050		mm
	v	3.6	7.4	11.9		μm
	Stress	915	1276	2298		MPa
Plastic contact to layer below	a	0.403	0.822	2.031		mm
	b	0.060	0.099	0.157		mm
	v	13.8	39.9	88.5		μm
At mid-loop and $\theta = 0$	δ_f	7.64	5.32	2.74	1.43	μm
	δ_j	1.78	−0.46	0.60	−0.016	μm
	η_j	0.54	0.86	0.34		μm
	$F_{j,j-1}$	11.02	8.05	33.6		N

$f = 30$ Hz; $y_{\max} = 635$ mm; tensile stress: aluminum—49.4 MPa, steel—218 MPa; strand tension: aluminum—443 N, steel—1955 N; bearing yield stress: aluminum—240 MPa.

The vector of displacements $\hat{\delta}, \hat{\eta}$ may be obtained by solution of Eq. (73). Table 2 presents results of a sample set of calculations.

4.6. Flexural rigidity

Using Eq. (62), the increment in tension in strand i of layer j is

$$\begin{aligned}\Delta T_{i,j} &= E_j A_j \cos\alpha_j \frac{\mathrm{d}}{\mathrm{d}x}\left[(\hat{\delta}_{f,j} - \hat{\delta}_j)\cos 2\pi\left(\frac{i-1}{n} \pm \frac{x}{\lambda}\right)\right],\\ &= \frac{2\pi E_j A_j}{\lambda_j}\cos\alpha_j(\hat{\delta}_{f,j} - \hat{\delta}_j)\sin 2\pi\left(\frac{i-1}{n} \pm \frac{x}{\lambda}\right).\end{aligned} \tag{74}$$

From Eq. (29),

$$\hat{\delta}_{f,j} = \frac{\kappa r_j \lambda_j}{2\pi}\cos\alpha_j. \tag{75}$$

Then

$$\Delta\hat{T}_j = -E_j A_j \cos\alpha_j\left(\kappa r_j \cos\alpha_j - \frac{2\pi}{\lambda_j}\hat{\delta}_j\right). \tag{76}$$

The bending moment arising from layer j is

$$M_j = \Delta\hat{T} r_j \cos\alpha_j \sum_{i=1}^{n_j} \sin^2\left[2\pi\left(\frac{i-1}{n_j} \pm \frac{x}{\lambda_j}\right)\right] = \frac{n_j}{2}\Delta\hat{T} r_j \cos\alpha_j. \tag{77}$$

Thus,

$$M_j = \frac{n_j}{2} r_j E_j A_j \cos^2\alpha_j\left(\kappa r_j \cos\alpha_j - \frac{2\pi}{\lambda_j}\hat{\delta}_j\right). \tag{78}$$

The flexural rigidity of the complete cable is

$$EI = \frac{1}{\kappa}\sum_{j=1}^{N} M_j + \frac{\pi}{64}\sum_{j=0}^{N} n_j E_j d_j^4. \tag{79}$$

$$EI = \frac{1}{\kappa}\sum_{j=1}^{N} \frac{n_j}{2} r_j E_j A_j \cos^2\alpha_j \left(\kappa r_j \cos\alpha_j - \frac{2\pi}{\lambda_j}\hat{\delta}_j\right) + \frac{\pi}{64}\sum_{j=0}^{N} n_j E_j d_j^4. \tag{80}$$

4.7. Forces at interstrand contacts

The tractions at the interlayer contacts between layers 1 and 2 were given by Eqs. (31) and (32). These equations may be put in generalized form by substituting j and $j+1$ for 1 and 2.

For the intralayer contacts of layer 1, let the angular position of the contact between strands i and $i+1$ be ρ_i. Then

$$\delta_{i+1} - \delta_i = \hat{\delta}_1\left[\cos\left(\rho_i + \frac{\pi}{n_1}\right) - \cos\left(\rho_i - \frac{\pi}{n_1}\right)\right] = -\hat{\delta}_1 \sin\rho_i \sin\frac{\pi}{n_1}. \tag{81}$$

Then the maximum interstrand traction per unit length is

$$\hat{\mathscr{F}}_{1.1} = -2\frac{\hat{\delta}_1}{C_x}\sin\frac{\pi}{n_1}. \tag{82}$$

Unlike interlayer traction, it occurs at $\rho_1 = \pm\pi/2$, on the top and bottom of the conductor.

4.8. Material damping at contacts

As noted earlier, measurements of damping at contacts [7,12] indicated material hysteresis to be a significant component, in fact the dominant one at low traction forces. This source of damping is generally characterized by specific damping ratio

$$\psi = J/U, \tag{83}$$

where J is the energy dissipated in an incremental volume of material per cycle and U is the strain energy stored in that volume at the point of maximum strain [21]. ψ is a function of the materials in contact. If they have different properties, its effective value is,

$$\psi_{j,j+1} = \frac{1}{C_{j,j+1}}\left(\psi_j\frac{2-\nu_j}{G_j} + \psi_{j+1}\frac{2-\nu_{j+1}}{G_{j+1}}\right). \tag{84}$$

The same definition applies to a body in which the strain is not uniform over its volume, and can be applied to a contact where the strain is concentrated in a small region. If ψ is known for a material, it has the same value for a body or a contact composed of that material. For a contact, the maximum stored energy is $U = \mathscr{F}^2 C/2$. However, for interlayer contacts, compliance C is different in the directions of the two principal axes. Thus,

$$J_{j,j+1} = \frac{\psi}{2}(C_{a,j,j+1}\mathscr{F}^2_{a,j,j+1} + C_{b,j,j+1}\mathscr{F}^2_{b,j,j+1}). \tag{85}$$

For the intralayer contacts of layer 1, dissipation per unit length is

$$J_{1,1} = \frac{\psi}{2} C_x \mathscr{F}^2_{1,1}. \tag{86}$$

Frictional dissipation at interlayer contacts between strands of the same material is given by Eq. (3) for the case where traction is in the direction of an ellipse principle axis. The case for other directions of loading does not appear to have been addressed in the literature. For present purposes we will assume that the effective

Table 3
Coefficients for calculation of frictional loss tangent for parallel strands.

b/d	0.00190	0.00286	0.00330	0.00369	0.00404
B	6310	6000	4380	3510	3000

traction force is the vector sum of $\mathscr{F}_{a,i,i+1}$ and $\mathscr{F}_{b,i,i+1}$. Then the contact dissipation becomes

$$W_{j,j+1}=\frac{(\mathscr{F}^2_{a,j,j+1}+\mathscr{F}^2_{b,j,j+1})^{3/2}}{36\mu_{j,j+1}P_{j,j+1}\sqrt{(ab)_{j,j+1}}}\left(\frac{2-\nu_j}{G_j}+\frac{2-\nu_{j+1}}{G_{j+1}}\right), \tag{87}$$

where provision is made for different materials in the contacting strands.

An analytical approach to frictional dissipation at parallel strand contacts also appears not to have been addressed in the literature. Measured values of the loss tangent for aluminum-to-aluminum strands of 1350-H19 alloy have been reported in the form

$$\sigma=B\frac{\delta}{d}, \tag{88}$$

for a range of values of theoretical b/d [19]. Values of B are listed in Table 3. The maximum stored energy per unit length of contact is $C_x\mathscr{F}^2_{1,1}/2$. Then, noting that $\delta=C_x\mathscr{F}_{1,1}$, frictional dissipation per unit length of contact is

$$W_{1,1}=\pi\frac{B}{d}C_x^2\mathscr{F}^3_{1,1}. \tag{89}$$

4.9. Conductor self damping

Dissipations given by Eqs. (85)–(89) are those that occur at individual contacts. These contacts are distributed around the girth of the layer according to θ, and along the conductor's length according to $\omega x/c$. For a conductor vibrating in sine-shaped loops as in Eq. (1) both distributions are sinusoidal. The J dissipations are proportional to $\mathscr{F}^2$ and thus to $\cos^2\theta\sin^2(\omega x/c)$. The mean of that distribution is $\frac{3}{8}$. The W dissipations are proportional to $\mathscr{F}^3$ and thus to $\cos^3\theta\sin^3(\omega x/c)$. The mean of that distribution is $\frac{5}{16}$. Thus, the total dissipation per unit length of conductor, averaged over a loop, is

$$\Delta\mathscr{E}=\frac{3}{8}\left(J_{1,1}+\sum_{j=1}^{N-1}N_{j,j+1}J_{j,j+1}\right)+\frac{5}{16}\left(W_{1,1}+\sum_{j=1}^{N-1}N_{j,j+1}W_{j,j+1}\right). \tag{90}$$

It is useful to express self damping as the ratio of dissipation to the maximum energy stored in flexure. Averaged over a loop maximum stored energy is

$$\mathscr{E}=\tfrac{1}{4}EI\kappa^2. \tag{91}$$

Then we may define the specific damping capacity of conductor stiffness as

$$\Psi=\frac{\Delta\mathscr{E}}{\mathscr{E}}=B_0+B_1\mathscr{K}. \tag{92}$$

Here we introduce the dimensionless curvature $\mathscr{K}$, defined as

$$\mathscr{K}=\frac{D}{2}\kappa. \tag{93}$$

It is equivalent to the bending strain of the conductor envelope at mid-loop. Substituting from Eqs. (85)–(89),

$$B_0=\frac{3}{2EI\kappa^2}\left[\psi_{1,1}C_x\hat{\mathscr{F}}^2_{1,1}+\sum_{j=1}^{N-1}\psi_{j,j+1}N_{j,j+1}(C_{a,j,j+1}\hat{\mathscr{F}}^2_{a,j,j+1}+C_{b,j,j+1}\hat{\mathscr{F}}^2_{b,j,j+1})\right], \tag{94}$$

$$B_1 = \frac{5}{2EI\kappa^3 D}\left[\pi\frac{B}{d}C_x^2\hat{\mathscr{F}}_{1,1}^3 + \sum_{j=1}^{N-1}\frac{N_{j,j+1}(\hat{\mathscr{F}}_{a,j,j+1}^2 + \hat{\mathscr{F}}_{b,j,j+1}^2)^{3/2}}{36\mu_{j,j+1}P_{j,j+1}\sqrt{(ab)_{j,j+1}}}\left(\frac{2-\nu_j}{G_j}+\frac{2-\nu_{j+1}}{G_{j+1}}\right)\right]. \quad (95)$$

B_0 pertains to material damping and B_1 to frictional damping.

5. Comparison with measured self-damping

5.1. Approach

Data on conductor self-damping is obtained through measurements in laboratory spans [4,5]. The data are presented as dissipation p_c in mw/m as a function of f and $y_{\max}$ for each combination of conductor size and tension tested. Fig. 11 shows a typical set of results [22]. Dissipation may also be calculated from the above analysis, utilizing Eqs. (91) and (92), as

$$p_c = f\Delta\mathscr{E} = f\Psi\mathscr{E} = f\frac{EI}{D^2}\mathscr{K}^2(B_0 + B_1\mathscr{K}). \quad (96)$$

Thus it should be possible to surmise B_0 and B_1 from measurements of p_c by expressing Eq. (96) as

$$B_0 + B_1\mathscr{K} = \frac{D^2}{fEI\mathscr{K}^2}p_c. \quad (97)$$

The parameter on the right, expressed as a function of $\mathscr{K}$, should define a linear function with intercept B_0 and slope B_1. However, EI is not generally known to the experimenter. It can be determined experimentally through Eq. (5) but that is not required by Refs. [4,5] and is seldom done.

It is helpful to define

$$c_0 = \frac{EI}{D^4}B_0 \quad \text{and} \quad c_1 = \frac{EI}{D^4}B_1. \quad (98)$$

Eq. (97) can then be expressed:

$$\frac{EI}{D^4}\Psi = c_0 + c_1\mathscr{K} = \frac{p_c}{fD^2\mathscr{K}^2} = \frac{H^2/m^2}{4\pi^4D^4f^5w_{\max}^2}p_c. \quad (99)$$

The parameter on the left is called the reduced specific damping capacity for flexure. The final step in Eq. (99) takes advantage of Eqs. (93) and (25). Then, if the parameter on the right is calculated from experimental data as a function of $\mathscr{K}$, its intercept and slope are c_0 and c_1, respectively. These values may be compared with predictions based on Eqs. (94), (95) and (98). Fig. 12 illustrates this process for the data that Fig. 11 was based

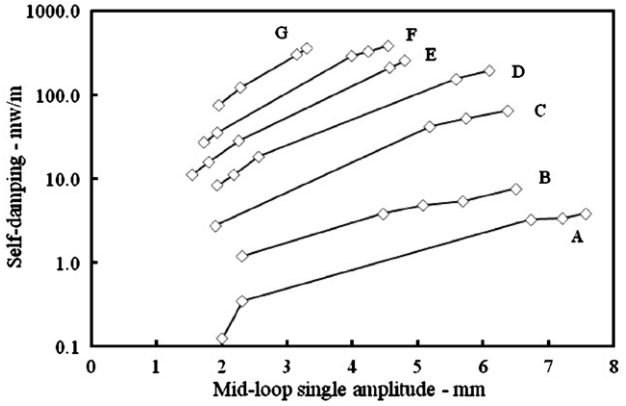

Fig. 11. Self-damping power, Hawk ACSR (26/7) at 20 percent of rated strength [22]. Frequencies: A–G—20.3, 24.0, 31.6, 37.3, 43.1, 49.1, 57.2 Hz, respectively.

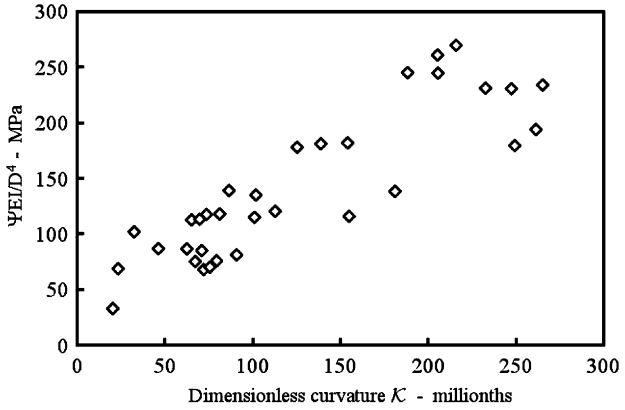

Fig. 12. Reduced specific flexural damping capacity for data of Fig. 11.

on. Regression of the data for Fig. 12 yields, $c_0 = 43\,\text{MPa}$ and $c_1 = 0.78\,\text{TPa}$. Note that c_0 and c_1, like B_0 and B_1, pertain to material damping and frictional damping, respectively.

5.2. Extraneous sources of damping in measured data

It is important to note that Eqs. (91) and (92) consider only damping internal to the conductor. Laboratory measurements of p_c include other sources of dissipation, and these must be subtracted from the raw data or avoided in the measurements. One source always present is fluid-dynamic damping by the air in the laboratory. This may be estimated and removed on the basis of Ref. [23]. A second source is localized sharp flexure at clamps at the span supports, so-called "end-point damping." This source may be eliminated from the data by employing the inverse standing wave ratio method rather than the power method [4] for the measurements. Alternatively, if the power method is used, the inverse standing wave ratio method may be used to determine the end point damping so that it can be subtracted from the raw data. Or, finally, end point damping may be minimized by use of flexures at the span terminations. The standards require that at least one of these options be employed.

A third source of external dissipation is transmission of energy through supports due to less-than-complete longitudinal rigidity there. This source, so-called "elongational damping," harnesses the small pulsations in conductor tension that accompany standing- wave vibration. It can be modeled as though it were elongational hysteresis in the conductor. Its magnitude is specific to the experimental setup and may be estimated by trial and error on the basis of its effectiveness in suppressing scatter in the estimated value of c_0.

5.3. Input parameters for analytical estimates

Analytical estimates of c_0 and c_1 from Eqs. (94), (95) and (98) rely upon knowledge of conductor structure (D, d_i, N, n_i, α_i, λ_i, m), its material properties (E_i, G_i, v_i, bearing yield stress), tension H and the conditions of vibration (f, $y_{\max}$). They also rely upon estimates of the strand tensions T_i and assumptions about coefficients of friction $\mu_{i,j}$ and the specific damping capacities ψ_i of the materials. The last three require some discussion.

In homogeneous conductors, strand tensions are well estimated by dividing H by the total number of strands in the conductor. In bimetallic conductors such as ACSR, and where different alloys are employed such as in aluminum conductor, aluminum alloy reinforced (ACAR), estimates of strand tensions must take into account nonlinear stress-strain characteristics of the aluminum portion and possibly its creep strain. A suitable procedure for this, known as the Alcoa Graphic Method, is described in Ref. [24] and computer programs for carrying out the calculations are available, e.g. Sag10 [25]. The estimated strand tension distributions are found to depend on the sequence of conductor tensions, and their durations, that have been applied to the conductor. Thus, the self-damping of a certain conductor at a tension of 15 percent of its rated

strength (RS) could be different depending upon whether or not it had previously been loaded to, say, 30 percent RS.

The coefficient of friction appropriate to Eqs. (3) and (87) is that of sliding. Measurements on contacting aluminum strands yield values ranging from 0.4 to 0.9 for as-drawn, mill quality samples, tested under oscillating traction at several crossing angles [22]. However the amplitudes of sliding in those tests, several mm, were much larger than those occurring at interstrand contacts during conductor vibration. Calculations based on the analysis of Section 4, and illustrated in Table 2, indicate that those amplitudes should not exceed a few microns. Thus, there is significant uncertainty as to what values of $\mu_{i,j}$ to employ.

There appears to be little applicable data on specific damping capacities ψ_i of materials used in overhead conductors, nor is it clear which of the several metallurgical mechanisms may be involved. Specific damping capacity ψ is in general a function of both temperature and frequency. Tests by Guan et al. [26] point toward values for aluminum in the region of 0.1 at 20 °C. However, the data were acquired at 1 Hz. Kaufman [27] reports values in the range 0.04–0.08 at about 25 Hz and room temperature.

5.4. Selection of measured self damping data

The next subsection presents a comparison of the analysis against several sets of self damping measurements. These sets were selected from a larger collection encompassing results from several laboratories. Most of the sets were acquired using the inverse standing wave ratio method, or using flexures at the supports to minimize end-point damping. However, two sets where the power method was employed without correction for end-point damping are included. It was possible to apply that correction on the basis of measurements of that damping, for the sizes of conductor involved, from another laboratory [22]. The selection was further limited based on the assumption that conductor self damping is indeed hysteretic and specific to energy stored by flexure. Then Ψ and, therefore, $\Psi EI/D^4$, should be a single-valued function of $\mathscr{K}$. Thus, the second selection criterion was whether the set yielded such a function when its data were plotted according to Eq. (99). A third criterion was whether estimated elongational damping was found to be small.

As noted in the introduction, the measurement process is difficult; scatter is to be expected. Fig. 12 reflects that reality. However, the collapse of the data of Fig. 11, with its span of three decades, into the 2:1 range of Fig. 12, supports the conclusion that this set of measurements meets the selection criterion. The other selected data sets displayed similar collapse. However, some sets had to be dropped because the range of $\mathscr{K}$ was too narrow to support estimates of c_0 and c_1. Details on the selected sets are listed in Table 4. The dimensions of the conductors involved are listed in Table 5.

5.5. Measurements versus the analytical model

Comparison of analytical estimates with measured data is hampered by uncertainties over coefficients of friction $\mu_{i,j}$, material specific damping ψ, and the division of tension between the aluminum and steel components of the conductor. Certain of the data sets came from tests where the conductor sample had been prestretched at a tension greater than the highest test tension for some period. Unfortunately, records of the actual prestress tension and its duration are no longer available. For purposes of this study, analytical estimates of c_0 and c_1 assumed that $\mu_{ij} = 0.6$, $\psi = 0.1$, and that the samples had been held for 4 days at test tension before the measurements.

Measured values of c_0 and c_1, derived from measured data through Eq. (99) from charts such as Fig. 12 are listed in Table 4, along with corresponding analytical estimates. The ratios of measured to analytical values of c_0 and c_1 are plotted as functions of conductor tension in percent of RS in Figs. 13 and 14, respectively. Measurements on the same sample at different tensions are connected by lines. The points and lines are coded to distinguish three groups.

One group, comprising four lines, is from tests where the conductor sample had been prestretched, i.e. held for several days at a tension equal to or greater than the highest test tension, before measurements were made. Due to the passage of time, information on specific tensions and their durations are no longer available and, for Items 4, 5 and 6 of Table 4, it has been *assumed* that the measurement sequence began with the highest tension. A second group comprising three lines represents tests where the conductor sample had been

Table 4
Comparison of measured and analytical estimates of c_0 and c_1.

Item	Ref.	Size	Stranding	Notes	H (% RS)	Measured		Analytical	
						c_0 (MPa)	c_1 (TPa)	c_0 (MPa)	c_1 (TPa)
1	[22]	Cardinal	54/7	a	15	48.5	0.317	39.1	1.043
2	[22]	Cardinal	54/7	a	25	85.2	0.297	35.0	0.626
3	[22]	Cardinal	54/7	a	30	85.4	0.312	33.5	0.519
4	[22]	Drake	26/7	b	30	24.3	1.303	45.5	0.756
5	[22]	Drake	26/7	b	35	0.0	1.647	44.1	0.651
6	[22]	Drake	26/7	b	40	12.1	1.868	42.9	0.572
7	[22]	Hawk S1	26/7	c	25	49.0	0.870	47.1	0.901
8	[22]	Hawk S2	26/7	c	20	36.4	0.806	49.1	1.114
9	[22]	Hawk S2	26/7	c	20	43.0	0.769	49.1	1.114
10	[22]	Hawk S2	26/7	c	25	66.0	0.590	47.1	0.901
11	[22]	Hawk S2	26/7	c	30	37.1	0.656	45.5	0.756
12	[22]	Hawk S2	26/7	c	35	58.2	0.624	44.1	0.651
13	[22]	Hawk S2	26/7	c	40	17.0	1.212	42.9	0.572
14	[22]	Hawk S3	26/7	c	15	33.2	0.492	51.6	1.454
15	[22]	Hawk S3	26/7	a,c	15	47.1	0.302	51.6	1.454
16	[22]	Hawk S3	26/7	a,c	20	82.5	0.324	49.1	1.114
17	[22]	Hawk S3	26/7	a,c	25	80.1	0.524	47.1	0.901
18	[22]	795 (63/19)	63/19		24	36.6	0.450	36.7	0.676
19	[28]	Eagle	30/7		26.5	13.2	0.425	41.5	0.809
20	[29]	Bersfort	48/7		15	72.8	0.696	44.8	1.561
21	[29]	Bersfort	48/7		20	43.7	0.787	42.0	1.140
22	[29]	Bersfort	48/7		25	46.1	0.615	39.9	0.892
23	[29]	Bersfort	48/7		30	41.2	0.629	38.2	0.728
24	[31]	Finch	54/19	b,d	15	104.3	1.863	41.1	1.061
25	[31]	Finch	54/19	b,d	20	99.5	0.873	38.3	0.773
26	[31]	Finch	54/19	b,d	25	64.0	0.637	36.3	0.606
27	[31]	Hawk	26/7	b,d	15	66.7	1.008	51.6	1.454
28	[31]	Hawk	26/7	b,d	20	50.7	0.688	49.1	1.114
29	[31]	Hawk	26/7	b,d	25	31.8	0.885	47.1	0.901
30	[30]	Hawk	26/7	b	10	160.1	1.721	55.0	2.073
31	[30]	Hawk	26/7	b	20	93.9	2.532	49.1	1.114
32	[30]	Hawk	26/7	b	30	89.8	1.844	45.5	0.756

Notes: (a) Sample was subjected to at least 24 hours of severe vibration; (b) sample was prestretched at high tension before testing; (c) S1, S2, S3 refer to samples 1, 2, 3; (d) end-point damping subtracted; provided from Ref. [22].

Table 5
Conductors represented in laboratory measurements.

Name	Area		Diameter (mm)	Stranding composition				Weight (kg/m)	Strength (kN)
	Aluminum (mm^2)	Total (mm^2)		Aluminum		Steel			
				No.	Diam.	No.	Diam. (mm)		
Hawk	242	281	21.79	26	3.44	7	2.68	0.978	86.7
Eagle	282	348	24.21	30	3.46	7	3.46	1.298	123.7
Drake	403	468	28.14	26	4.44	7	3.47	1.628	140.1
	403	638	28.52	63	2.85	19	2.27	1.724	186.8
Cardinal	483	546	30.78	54	3.38	7	3.38	1.829	150.4
Finch	564	635	32.84	54	3.65	19	2.19	2.130	173.9
Bersfort	686	747	35.6	48	4.3	7	3.3	2.37	180.1

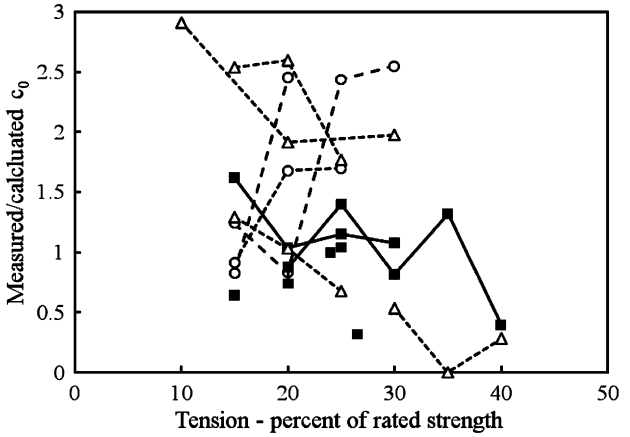

Fig. 13. Ratio of measured to calculated c_0 (material damping). Squares: unseasoned group. Triangles: prestretched group. Circles: vibration aged.

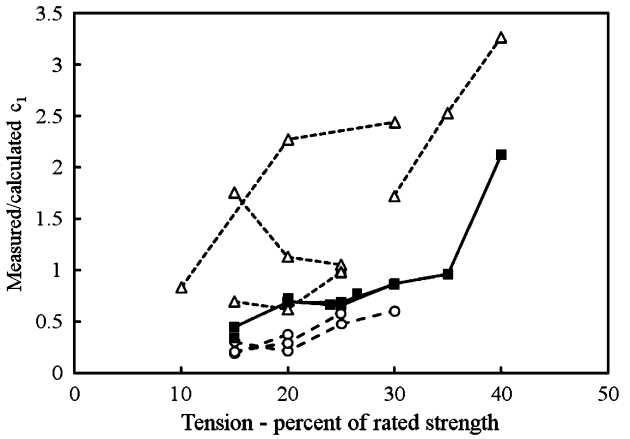

Fig. 14. Ratio of measured to calculated c_1 (frictional damping). Squares: unseasoned group. Triangles: prestretched group. Circles: vibration aged.

"vibration-aged", i.e. exposed to at least 24 hours of severe vibration, prior to testing. The tests in the third group were not reported to have received either pre-measurement treatment; their samples were "unseasoned".

The ratios of measured to analytical values of c_0 are plotted in Fig. 13. For the unseasoned group, the ratios cluster around unity and do not display a trend with respect to tension. Ratios for the tests preceded by vibration aging or prestretching tend to deviate on the high side from the unseasoned samples. Lines for the vibration aged group indicate positive trends with increasing tension. Those for the prestretched group indicate negative trends. Overall, correlation between measured and analytical values of c_0 extends only as far as order of magnitude.

Ratios of measured to analytical values of c_1 are plotted in Fig. 14. The unseasoned group appears to correlate well within itself, and to define a function that rises with conductor tension. Over the range from 20 to 35 percent RS, the correlation between measured and analytical values of c_1 may be considered good, considering the uncertainties affecting several parameters involved in the analysis. The measured to analytical ratios for the vibration aged group are consistently low compared with the unseasoned group, while those for the prestretched group are almost entirely on the high side, and generally by a substantial margin.

6. Discussion

It is clear from the comparisons in Figs. 13 and 14 that there are deficiencies in the analytical approach. These may lie in the structure of the analysis, in assumptions and approximations, or in the quality of input data. By and large, they point to the need for further research. The following comments concern the directions those efforts might take.

6.1. Unseasoned group

It is helpful to begin with the area where correlation between measurement and analysis was best: the unseasoned group. The ratios of measured to analytical values of c_0 are plotted in Fig. 13. c_0 pertains to material damping, assumed to be hysteretic. As noted earlier, there is a paucity of data on material specific damping capacity ψ for overhead conductor aluminum alloys in the temperature and frequency ranges of interest. The c_0 ratios for the unseasoned group cluster around unity. Their average is 0.96, and standard deviation is 0.36, tending to support the casually assumed value, $\psi = 0.1$.

As noted above, there is good correlation between measured and analytical estimates of c_1 in the tension range 20–35 percent RS indicating that in that area, at least, the analytical structure, with its assumptions and approximations, is sound. Thus the deviation between measurement and analysis is likely due to input data. Examination of Eq. (87) suggests coefficient of friction μ as a source. The analysis used $\mu = 0.6$, resulting in a c_1 ratio ranging from 0.7 to 1.0. Had the analysis used $\mu = 0.71$, well within the range of doubt, the ratio would have ranged from 0.81 to 1.19. Thus, more refined measurements of coefficients of friction, particularly at very small amplitudes of sliding, would be helpful.

Eq. (87) is also affected by the estimated sizes of the interstrand contacts. As discussed in Section 4.2, and illustrated in Table 2, the normal loads on these contacts put them well into the plastic region. The bearing yield strength has been used to estimate contact areas. However, the data of Fig. 4 show that average contact stress at low normal loads is smaller than the 240 MPa used in the calculations. Finite element studies by Hardy et al. [32] show that the uniform distribution of pressure over the contact area, assumed in the analysis, is only realized when the contact is well into the plastic regime. In early stages of that regime, average pressure is significantly less than the yield stress. The effect is that, at the smaller normal loads that occur at lower tensions, the contact areas would be larger than estimated, leading to reduced $W_{j,j+1}$ and, therefore, reduced B_1 and c_1. This would raise the unseasoned points at 15 percent RS in Fig. 14 toward unity. The analytical approach would be improved by better modeling of the lower contact loadings.

6.2. Prestretched group

The highest-tension point in the unseasoned group in Fig. 14 displays a sharp rise in the c_1 ratio, indicating that the analysis substantially underestimates c_1. This deviation is shared by most of the points in the prestretched group. Evidently, effects of exposure to high conductor tension take actual conductors beyond the limits of the analytical treatment. It seems likely that the pertinent assumption is that the pressure between strands of a given layer remains zero. Standards governing conductor fabrication assure that, as manufactured, any layer with more than seven strands does not fill the circumferential space allotted to it. In fact, if preferred lay ratios are used, there is very nearly 1 percent of extra space in the outer layer of ACSR.

When conductors are tensioned, relative normal displacements h of the interlayer contacts occur. These cause the conductor diameter to shrink. The amount of shrinkage can be estimated by accumulating the displacements layer-by-layer. Examples of these displacements were given in Table 2, for both purely elastic and purely plastic strains. The displacements for the plastic regime were estimated using an assumed model that is, as noted earlier, plausible but unproven. The estimates are thus somewhat speculative. Calculations using that model indicate that when tension reaches about 30 percent RS conductor diameter has decreased enough to eliminate the extra space in the outer layer. At that point the lateral displacements η are forced to zero, and any further increase in tension results in intralayer pressures between strands. These pressures would have two effects. One would be to activate frictional and hysteretic damping *within* layers. The other would be to relieve the interlayer contacts of some of the pressure predicted by Eq. (11). Contact area would then be

reduced, leading to increased hysteretic and frictional damping there. Subsequent reduction in tension would leave the plastic deflections in place, so these effects would tend to persist.

Analysis of these effects is beyond the scope of the present paper. It might be possible to estimate the shift in the interstrand pressure distribution, albeit with limited confidence. However, the intralayer frictional movements would involve gross sliding, requiring more complex dissipation models than Eqs. (3) and (86). Prestretching is an area that invites further research.

6.3. Vibration-aged group

The three lines for c_1 ratio in the vibration-aged samples in Fig. 14 lie significantly below the unseasoned group, indicating that the analysis overestimated frictional damping. It appears that exposure to severe vibration affected the interlayer contacts. Eq. (87) suggests that the coefficient of friction was substantially increased and/or the contact area was expanded. Laboratory study of contact wear for very small relative movements is needed. Johnson has already done this for contact between a hard steel ball and hard steel plate [12]. He found evidence that, even without gross sliding, fretting damage occurred in the annular region at the edge of the contact where there was microslip. The coefficient of friction in the fretted region appeared to increase to a value about double that of a fresh surface. This could account for at least part of the deviation of this group from the unseasoned group. Fretting behavior of aluminum is not necessarily the same as that of steel, so a separate testing program is indicated to develop this possibility.

The c_0 ratios for the vibration aged group tend to deviate on the high side of those for the unseasoned samples, suggesting that fretting damage caused an increase in ψ. Fretting in aluminum is known to produce a layer of disturbed material composed of finely divided particles of aluminum, permeated with aluminum oxide [33,34]. This layer is somewhat spongy, so increased damping capacity is reasonable. The aging was applied at the lowest test tension, so the fretting occurred in a small contact area. Note in Fig. 13 that the measured value of c_0 increased as tension increased. This increase could be explained on the basis that, as increasing tension caused the contact to expand, the spongy fretted region was absorbed into the no-slip area of the contact where material damping takes place.

7. Conclusions

The analytical model described in the paper connects the behavior of the composite conductor with the basic mechanisms thought to be involved in self-damping: material damping and micro-friction at interstrand contacts. The model yields estimates of self-damping that are in reasonable agreement with measured data within a limited range. Cases where agreement is poor appear to be associated with treatments applied to the conductor samples involved in the measurements prior to testing. The specific treatments are exposure to severe vibration, and exposure to higher-than-normal tension for some period. Possible mechanisms by which these treatments produce their effects are described, offering direction to further research.

Appendix A. Polynomials for functions used in Eqs. (13), (15) and (19)

Function	p	q	g	$\Gamma(a/b,\nu)$ Transverse	$\Gamma(a/b,\nu)$ Parallel
Argument	ξ	ξ	ξ	a/b	a/b
v_0	1.88711E+01	1.62280E−01	1.22969E−01	5.14839E−01	4.20504E−01
v_1	−1.32533E+02	1.02588E+00	1.38237E+00	3.89839E−01	4.95105E−01
v_2	5.14558E+02	−1.06150E+00	−1.65436E+00	−5.81438E−02	−6.96486E−02
v_3	−1.09125E+03	4.92256E−02	1.36152E+00	4.78148E−03	5.57749E−03
v_4	1.18555E+03	1.79314E+00	−6.38800E−01	−1.87643E−04	−2.15874E−04
v_5	−5.15439E+02	−1.44525E+00	1.20246E−01	2.72816E−06	3.11405E−06

Polynomials take the form, $\sum_{i=0}^{5} v_i \arg^i$. p, q, g are valid for ξ less than 0.7 radians.
$v = 0.33$.

References

[1] J.S. Tompkins, L.L. Merrill, B.L. Jones, Quantitative relationships in conductor vibration damping, *Transactions of the American Institute of Electrical Engineers, Part III. Power Apparatus and Systems* 75 (1956) 879–896.
[2] C.B. Rawlins, Wind tunnel measurements of the power imparted to a model of a vibrating conductor, *Institute of Electrical and Electronics Engineers Transactions on Power Apparatus and Systems* PAS-102 (4) (1983) 963–971.
[3] Institute of Electrical and Electronics Engineers, IEEE Standard 664-1993, Guide on the Measurement of the Performance of Aeolian Vibration Dampers for Single Conductors, 1993.
[4] Institute of Electrical and Electronics Engineers, IEEE Standard 563-1993, Guide on Conductor Self-damping Measurements, 1978.
[5] International Conference on Large High Voltage Electric Systems, Guide on Conductor Self-Damping Measurements, *Electra*, No. 62, 1979, pp. 79–90.
[6] P.J. Ryle, Conductor vibration, *Proceedings of the Institution of Electrical Engineers*, December 1930, pp. 7–22.
[7] R.D. Mindlin, W.P. Mason, J.F. Osmer, H. Deresiewicz, Effects of an oscillating tangential force on the contact surfaces of elastic spheres, *Proceedings of the First US National Congress of Applied Mechanics*, ASME, New York, 1951, pp. 203–208.
[8] K.L. Johnson, *Contact Mechanics*, Cambridge University Press, Cambridge, 1985.
[9] L.E. Goodman, C.B. Brown, Energy dissipation in contact friction: constant normal and cyclic tangential loading, *Journal of Applied Mechanics* 1 (1962) 17–22.
[10] C. Hardy, A. Leblond, S. Goudreau, L. Cloutier, Application of contact mechanics to cable self-damping, *Proceedings of the Third International Symposium on Cable Dynamics*, Trondheim, Norway, 16–18 August 1999, pp. 1–6.
[11] C. Hardy, A. Leblond, On the dynamic flexural rigidity of taut stranded cables, *Proceedings of the Fourth International Symposium on Cable Dynamics*, Santa Margherita Ligure, Italy, 15–18 September 2003, pp. 45–52.
[12] K.L. Johnson, Energy dissipation at spherical surfaces in contact transmitting oscillating forces, *Journal of Mechanical Engineering Science* 3 (4) (1961) 362–368.
[13] American Society for Testing and Materials, ASTM Standards on Metallic Electrical Conductors, PCN 01-020385-22, 1985.
[14] C.B. Rawlins, *Analytical Elements of Overhead Conductor Fabrication*, Fultus Books, Palo Alto, CA, 2005.
[15] L.A. Pipes, Cable and Damper Vibration Studies, *Transactions of the American Institute of Electrical Engineers* 55 (1936) 600–614.
[16] W.C. Young, *Roark's Formulas for Stress & Strain*, sixth ed., McGraw-Hill, New York, 1989 (Table 33.4).
[17] A.E.H. Love, *A Treatise on the Mathematical Theory of Elasticity*, Dover, New York, 1944 (Section 137).
[18] R.D. Mindlin, Compliance of elastic bodies in contact, *Journal of Applied Mechanics* 16 (1949) 259–268.
[19] C.B. Rawlins, Measurements of interstrand contact damping for parallel strands, *Proceedings of the International Seminar on Cable Dynamics*, Japan Society for Wind Engineering, Tokyo, Japan, 13 October 1997, pp. 121–127.
[20] International Electrotechnical Commission, IEC Publications 207–210, Geneva, 1966.
[21] B.J. Lazan, *Damping of Materials and Members in Structural Mechanics*, Pergamon Press, New York, 1968.
[22] Data courtesy of ACA Conductor Accessories (former Alcoa).
[23] C.B. Rawlins, Measurements of Fluid-dynamic Damping of Stranded Cable Models at Low Oscillation Amplitudes, Technical Paper No. 27, Alcoa Conductor Products Company, April 1990.
[24] Aluminum Association, *Aluminum Electrical Conductor Handbook*, second ed., 1982.
[25] 〈http://www.sag10.com〉 (accessed 15.04.08).
[26] X.S. Guan, H. Numakura, M. Koiwa, Internal Friction Peak in Cold-worked "Pure" Aluminum and Aluminum Alloys, *Journal de Physique-IV*, Colloque C8, supplement au *Journal de Physique—III* 6 (1966) C8-219–C8-222.
[27] J.G. Kaufman, Damping in light metals, *Materials in Design Engineering* 56 (2) (1962) 104–105.
[28] G. Diana, M. Falco, A. Cigada, A. Manenti, On the measurement of over head transmission lines conductor self-damping, *Institute of Electrical and Electronics Engineers Transactions on Power Delivery* 15 (1) (2000) 285–292.
[29] D. Noiseux, Complete measurements of the internal damping of Bersfort Conductor, Laws of similitude of ACSR conductors (in French), Report IREQ-4402, Institut de recherché d'Hydro-Quebéc, March 1989.
[30] *International Conference on Large High Voltage Electric Systems*, Conductor Self-damping, Working Group Report 22-94(WG-11)-126, August 1994 (Tables 10–12 (RIBE)).
[31] M. Estarellas, Conductor self-damping measurements according to the CIGRE/IEEE guide, Working Group Document 22-82(WG01)-6, *International Conference on Large High Voltage Electric Systems*, May 1982.
[32] C. Hardy, C.N. Baronet, G.V. Tordion, The elasto-plastic indentiation of a hal-space by a rigid sphere, *International Journal for Numerical Methods in Engineering* 3 (1971) 451–462.
[33] W.G. Fricke Jr., C.B. Rawlins, Importance of fretting in vibration failures of stranded conductors, *American Institute of Electrical Engineers Transactions on Power Apparatus and Systems* PAS-87 (6) (1968) 1381–1384.
[34] L. Möcks, Vibration damage in overhead conductors, *Bulletin of the Swiss Electrotechnical Association* 69 (5) (1970) 223–227 (in German).